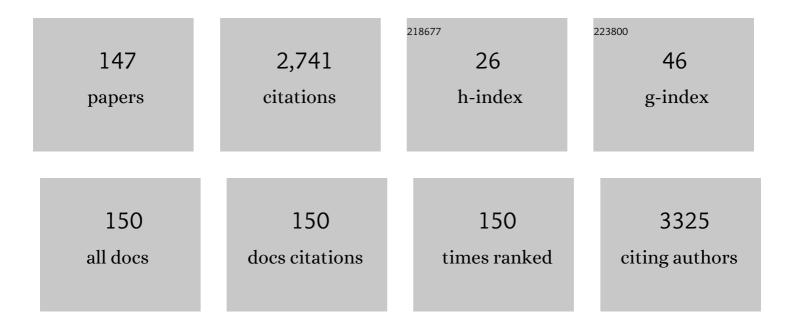
List of Publications by Year in descending order

Source: https://exaly.com/author-pdf/5592525/publications.pdf Version: 2024-02-01



#	Article	IF	CITATIONS
1	Measurements of the Lamb-Mössbauer factor at simultaneous high-pressure-temperature conditions and estimates of the equilibrium isotopic fractionation of iron. American Mineralogist, 2022, 107, 421-431.	1.9	5
2	Self-consistent thermodynamic parameters of pyrope and almandine at high-temperature and high-pressure conditions: Implication on the adiabatic temperature gradient. Physics of the Earth and Planetary Interiors, 2022, 322, 106789.	1.9	5
3	The role of intrinsic stacking fault in facilitating the pressure-induced phase transition in CoCrFeMnNi high entropy alloys. Materials Chemistry and Physics, 2022, 275, 125273.	4.0	2
4	Thermal equation of state of F-bearing superhydrous phase B (Mg10Si3O14(OH,F)4): Implications for the transportation of fluorine and water into the lower mantle. Physics of the Earth and Planetary Interiors, 2022, 323, 106824.	1.9	1
5	Effect of Thermoelastic Properties of the Pyrope-Almandine Solid Solutions on the Entrapment Pressure of Garnet-Related Elastic Geobarometer. Frontiers in Earth Science, 2022, 9, .	1.8	0
6	High-Pressure Investigation of 2,4,6-Trinitro-3-bromoanisole (TNBA): Structural Determination and Piezochromism. Journal of Physical Chemistry C, 2022, 126, 1176-1187.	3.1	5
7	Phase Transitions of Feâ€, Al―and Caâ€Bearing Orthopyroxenes at High Pressure and High Temperature: Implications for Metastable Orthopyroxenes in Stagnant Slabs. Journal of Geophysical Research: Solid Earth, 2022, 127, .	3.4	2
8	Negative linear compressibility in Se at ultra-high pressure above 120 GPa. IUCrJ, 2022, 9, 253-260.	2.2	3
9	Mechanochemical Synthesis of Nanocrystalline Olivine-Type Mg2SiO4 and MgCoSiO4. Crystals, 2022, 12, 369.	2.2	1
10	Thermal equation of state of the main minerals of eclogite: Constraining the density evolution of eclogite during the delamination process in Tibet. Solid Earth, 2022, 13, 745-759.	2.8	1
11	Partnership for eXtreme Xtallography (PX2)—A state-of-the-art experimental facility for extreme-conditions crystallography: A case study of pressure-induced phase transition in natural ilvaite. Matter and Radiation at Extremes, 2022, 7, .	3.9	4
12	Melting and phase relations of Fe-Ni-Si determined by a multi-technique approach. Earth and Planetary Science Letters, 2022, 584, 117358.	4.4	4
13	Tracing electron density changes in langbeinite under pressure. IUCrJ, 2022, 9, 146-162.	2.2	4
14	Super-hydration and reduction of manganese oxide minerals at shallow terrestrial depths. Nature Communications, 2022, 13, 1942.	12.8	5
15	Drastic enhancement of magnetic critical temperature and amorphization in topological magnet EuSn2P2 under pressure. Npj Quantum Materials, 2022, 7, .	5.2	9
16	Topological Ordering of Memory Glass on Extended Length Scales. Journal of the American Chemical Society, 2022, 144, 7414-7421.	13.7	8
17	Recent developments on high-pressure single-crystal X-ray diffraction at the Partnership for eXtreme Xtallography (PX2) program. Physics and Chemistry of Minerals, 2022, 49, .	0.8	3
18	Coexistence of vitreous and crystalline phases of H ₂ O at ambient temperature. Proceedings of the National Academy of Sciences of the United States of America, 2022, 119, .	7.1	3

#	Article	IF	CITATIONS
19	Equation of state of elbaite at high pressure up to 21.1 GPa and room temperature. Physics and Chemistry of Minerals, 2022, 49, .	0.8	1
20	Regulating off-centering distortion maximizes photoluminescence in halide perovskites. National Science Review, 2021, 8, nwaa288.	9.5	70
21	The effect of nitrogen on the compressibility and conductivity of iron at high pressure. Geoscience Frontiers, 2021, 12, 983-989.	8.4	14
22	Thermoelasticity and stability of natural epidote at high pressure and high temperature: Implications for water transport during cold slab subduction. Geoscience Frontiers, 2021, 12, 921-928.	8.4	7
23	Constraining the density evolution during destruction of the lithospheric mantle in the eastern North China Craton. Gondwana Research, 2021, 91, 18-30.	6.0	5
24	Enhanced Photocurrent of All-Inorganic Two-Dimensional Perovskite Cs ₂ Pbl ₂ Cl ₂ via Pressure-Regulated Excitonic Features. Journal of the American Chemical Society, 2021, 143, 2545-2551.	13.7	79
25	Room temperature facile synthesis of olivine-Co ₂ SiO ₄ nanoparticles utilizing a mechanochemical method. RSC Advances, 2021, 11, 20687-20690.	3.6	5
26	Thermal equation of state of phase egg (AlSiO3OH): implications for hydrous phases in the deep earth. Contributions To Mineralogy and Petrology, 2021, 176, 1.	3.1	2
27	Pressure-induced ferroelectric-like transition creates a polar metal in defect antiperovskites Hg3Te2X2 (X = Cl, Br). Nature Communications, 2021, 12, 1509.	12.8	14
28	Ultra-incompressible High-Entropy Diborides. Journal of Physical Chemistry Letters, 2021, 12, 3106-3113.	4.6	17
29	From Semiconducting to Metallic: Jahn–Teller-Induced Phase Transformation in Skyrmion Host GaV4S8. Journal of Physical Chemistry C, 2021, 125, 5771-5780.	3.1	7
30	Microscopic phase diagram of Eu(Fe1â^'xNix)As2 (x = 0,0.04) under pressure. Physical Review B, 2021, 103,	3.2	5
31	Regulating Exciton–Phonon Coupling to Achieve a Nearâ€Unity Photoluminescence Quantum Yield in Oneâ€Dimensional Hybrid Metal Halides. Advanced Science, 2021, 8, e2100786.	11.2	61
32	Effect of structural water on the elasticity of orthopyroxene. American Mineralogist, 2021, , .	1.9	1
33	Highâ€Pressure Phase Stability and Thermoelastic Properties of Iron Carbonitrides and Nitrogen in the Deep Earth. Journal of Geophysical Research: Solid Earth, 2021, 126, e2021JB021934.	3.4	3
34	A large enhancement of ionic conductivity in SrCoO2.5 controlled by isostructural phase transition and negative linear compressibility. Applied Physics Letters, 2021, 119, .	3.3	2
35	The Water-Fe-Pressure dependent single-crystal elastic properties of wadsleyite: Implications for the seismic anisotropy in the upper Mantle Transition Zone. Earth and Planetary Science Letters, 2021, 565, 116955.	4.4	10
36	Experimental calibration of the reduced partition function ratios of tetrahedrally coordinated silicon from the Debye–Waller factors. Contributions To Mineralogy and Petrology, 2021, 176, 1.	3.1	3

#	Article	IF	CITATIONS
37	High Pressure Behaviors and a Novel High-Pressure Phase of Cuprous Oxide Cu2O. Frontiers in Earth Science, 2021, 9, .	1.8	0
38	Structural and electronic phase transition in Bi2Se2.1Te0.9 under pressure. Journal of Physics and Chemistry of Solids, 2021, 156, 110123.	4.0	1
39	Phase transition mechanism and bandgap engineering of Sb2S3 at gigapascal pressures. Communications Chemistry, 2021, 4, .	4.5	16
40	Phase Transitions in Natural Vanadinite at High Pressures. Minerals (Basel, Switzerland), 2021, 11, 1217.	2.0	0
41	High-pressure crystal structure and equation of state of ferromagnesian jeffbenite: implications for stability in the transition zone and uppermost lower mantle. Contributions To Mineralogy and Petrology, 2021, 176, 1.	3.1	1
42	Self-Consistent Thermodynamic Parameters of Diopside at High Temperatures and High Pressures: Implications for the Adiabatic Geotherm of an Eclogitic Upper Mantle. Minerals (Basel, Switzerland), 2021, 11, 1322.	2.0	2
43	Grain size dependent high-pressure elastic properties of ultrafine micro/nanocrystalline grossular. Scientific Reports, 2021, 11, 22481.	3.3	0
44	Boron-Rich Molybdenum Boride with Unusual Short-Range Vacancy Ordering, Anisotropic Hardness, and Superconductivity. Chemistry of Materials, 2020, 32, 459-467.	6.7	35
45	An Isosymmetric High-Pressure Phase Transition in α-Glycylglycine: A Combined Experimental and Theoretical Study. Journal of Physical Chemistry B, 2020, 124, 1-10.	2.6	14
46	High-Pressure Phase Transitions in Densely Packed Nanocrystallites of TiO ₂ -II. Journal of Physical Chemistry C, 2020, 124, 1197-1206.	3.1	4
47	Elastic and magnetic properties of Fe3P up to core pressures: Phosphorus in the Earth's core. Earth and Planetary Science Letters, 2020, 531, 115974.	4.4	14
48	Topaz, a Potential Volatile-Carrier in Cold Subduction Zone: Constraint from Synchrotron X-ray Diffraction and Raman Spectroscopy at High Temperature and High Pressure. Minerals (Basel,) Tj ETQq0 0 0 rgBT	/Qverlock	1 © Tf 50 29
49	Pressure-Induced Phase Transition in Mn(Ta,Nb) ₂ O ₆ : An Experimental Investigation and First-Principle Study. Inorganic Chemistry, 2020, 59, 18122-18130.	4.0	6
50	A new hydrous iron oxide phase stable at mid-mantle pressures. Earth and Planetary Science Letters, 2020, 550, 116551.	4.4	5
51	Spin Transitions and Compressibility of εâ€Fe 7 N 3 and γ′â€Fe 4 N: Implications for Iron Alloys in Terrestrial Planet Cores. Journal of Geophysical Research: Solid Earth, 2020, 125, e2020JB020660.	3.4	4
52	Pressure-Induced Selective Amorphization of CsPbBr ₃ for the Purification of Cs ₄ PbBr ₆ . Journal of Physical Chemistry C, 2020, 124, 22291-22297.	3.1	9
53	Pressure-stabilized divalent ozonide CaO3 and its impact on Earth's oxygen cycles. Nature Communications, 2020, 11, 4702.	12.8	20
54	Potential Interaction of Noble Gas Atoms and Anionic Electrons in Ca ₂ N. Journal of Physical Chemistry C, 2020, 124, 12213-12219.	3.1	3

#	Article	IF	CITATIONS
55	From Sodium–Oxygen to Sodium–Air Battery: Enabled by Sodium Peroxide Dihydrate. Nano Letters, 2020, 20, 4681-4686.	9.1	31
56	Phase Transition of Enstatiteâ€Ferrosilite Solid Solutions at High Pressure and High Temperature: Constraints on Metastable Orthopyroxene in Cold Subduction. Geophysical Research Letters, 2020, 47, e2020GL087363.	4.0	12
57	The seismically fastest chemical heterogeneity in the Earth's deep upper mantle—implications from the single-crystal thermoelastic properties of jadeite. Earth and Planetary Science Letters, 2020, 543, 116345.	4.4	7
58	Pressure-driven chemical lock-in structure and optical properties in Sillen compounds PbBiO ₂ X (X = Cl, Br, and I). Journal of Materials Chemistry A, 2020, 8, 13610-13618.	10.3	12
59	An Externally-Heated Diamond Anvil Cell for Synthesis and Single-Crystal Elasticity Determination of Ice-VII at High Pressure-Temperature Conditions. Journal of Visualized Experiments, 2020, , .	0.3	12
60	Elasticity of single-crystal Fe-enriched diopside at high-pressure conditions: Implications for the origin of upper mantle low-velocity zones. American Mineralogist, 2020, 105, 363-374.	1.9	5
61	Coesite Formation at Low Pressure during Supersonic Microprojectile Impact of Opal. ACS Earth and Space Chemistry, 2020, 4, 1291-1297.	2.7	6
62	Pressure-Induced Superconductivity in the Wide-Band-Gap Semiconductor Cu2Br2Se6 with a Robust Framework. Chemistry of Materials, 2020, 32, 6237-6246.	6.7	6
63	Deviatoric stress-induced quasi-reconstructive phase transition in ZnTe. Journal of Materials Chemistry C, 2020, 8, 3795-3799.	5.5	8
64	Structure and Behavior of the Ni End-Member Schreibersite Ni3P under Compression to 50 GPa. Minerals (Basel, Switzerland), 2020, 10, 306.	2.0	2
65	Raman and X-ray diffraction study of pressure-induced phase transition in synthetic Mg2TiO4. Scientific Reports, 2020, 10, 6278.	3.3	2
66	Investigation of the crystal structure of a low water content hydrous olivine to 29.9 GPa: A high-pressure single-crystal X-ray diffraction study. American Mineralogist, 2020, 105, 1857-1865.	1.9	7
67	Experimental Evidence for Partially Dehydrogenated ε-FeOOH. Crystals, 2019, 9, 356.	2.2	3
68	Elasticity of single-crystal low water content hydrous pyrope at high-pressure and high-temperature conditions. American Mineralogist, 2019, 104, 1022-1031.	1.9	9
69	Origin and consequences of non-stoichiometry in iron carbide Fe7C3. American Mineralogist, 2019, 104, 325-332.	1.9	2
70	<i>In Situ</i> Formed Ir ₃ Li Nanoparticles as Active Cathode Material in Li–Oxygen Batteries. Journal of Physical Chemistry A, 2019, 123, 10047-10056.	2.5	11
71	Pressure-Induced Superconductivity and Flattened Se ₆ Rings in the Wide Band Gap Semiconductor Cu ₂ I ₂ Se ₆ . Journal of the American Chemical Society, 2019, 141, 15174-15182.	13.7	9
72	Structural Phase Transition, Optical and Electrical Property Evolutions of Thiospinel AgIn ₅ S ₈ under High Pressure. Inorganic Chemistry, 2019, 58, 12628-12634.	4.0	12

#	Article	IF	CITATIONS
73	Synthesis of Manganese Mononitride with Tetragonal Structure under Pressure. Crystals, 2019, 9, 511.	2.2	3
74	Highâ€Pressure Singleâ€Crystal Elasticity and Thermal Equation of State of Omphacite and Their Implications for the Seismic Properties of Eclogite in the Earth's Interior. Journal of Geophysical Research: Solid Earth, 2019, 124, 2368-2377.	3.4	13
75	Elasticity of single-crystal periclase at high pressure and temperature: The effect of iron on the elasticity and seismic parameters of ferropericlase in the lower mantle. American Mineralogist, 2019, 104, 262-275.	1.9	27
76	Green Emitting Single-Crystalline Bulk Assembly of Metal Halide Clusters with Near-Unity Photoluminescence Quantum Efficiency. ACS Energy Letters, 2019, 4, 1579-1583.	17.4	117
77	Tunable photoluminescence and an enhanced photoelectric response of Mn ²⁺ -doped CsPbCl ₃ perovskite nanocrystals <i>via</i> pressure-induced structure evolution. Nanoscale, 2019, 11, 11660-11670.	5.6	15
78	High-pressure behavior of liebenbergite: The most incompressible olivine-structured silicate. American Mineralogist, 2019, 104, 580-587.	1.9	4
79	Pressure-induced magnetovolume effect in CoCrFeAl high-entropy alloy. Communications Physics, 2019, 2, .	5.3	16
80	Pressure-induced polymorphism and piezochromism in Mn2FeSbO6. Applied Physics Letters, 2019, 114, 162903.	3.3	6
81	Pressure-induced fluorescence enhancement of FA _α PbBr _{2+α} composite perovskites. Nanoscale, 2019, 11, 5868-5873.	5.6	16
82	Pressure-Induced Phase Transitions of Natural Brookite. ACS Earth and Space Chemistry, 2019, 3, 844-853.	2.7	5
83	Enhanced Néel temperature in EuSnP under pressure. Dalton Transactions, 2019, 48, 5327-5334.	3.3	3
84	Deviatoric deformation kinetics in high entropy alloy under hydrostatic compression. Journal of Alloys and Compounds, 2019, 792, 116-121.	5.5	13
85	Hydrogen Effect on the Sound Velocities of Upper Mantle Omphacite. Minerals (Basel, Switzerland), 2019, 9, 690.	2.0	1
86	Compressibility of synthetic Mg-Al tourmalines to 60 GPa. American Mineralogist, 2019, 104, 1005-1015.	1.9	11
87	Crystal-Chemical Properties of Synthetic Almandine-Pyrope Solid Solution by X-Ray Single-Crystal Diffraction and Raman Spectroscopy. Crystals, 2019, 9, 541.	2.2	3
88	Nixonite, Na2Ti6O13, a new mineral from a metasomatized mantle garnet pyroxenite from the western Rae Craton, Darby kimberlite field, Canada. American Mineralogist, 2019, 104, 1336-1344.	1.9	3
89	A New High-Pressure Phase Transition in Natural Gedrite. Crystals, 2019, 9, 521.	2.2	2
90	Single-crystal X-ray diffraction of grunerite up to 25.6ÂGPa: a new high-pressure clinoamphibole polymorph. Physics and Chemistry of Minerals, 2019, 46, 215-227.	0.8	8

#	Article	IF	CITATIONS
91	Structure-Controlled Oxygen Concentration in Fe ₂ O ₃ and FeO ₂ . Inorganic Chemistry, 2019, 58, 5476-5482.	4.0	10
92	Pressure-induced dehydration of dioptase: A single-crystal X-ray diffraction and Raman spectroscopy study. Comptes Rendus - Geoscience, 2019, 351, 121-128.	1.2	0
93	Thermoelastic Properties of Eclogitic Garnets and Omphacites: Implications for Deep Subduction of Oceanic Crust and Density Anomalies in the Upper Mantle. Geophysical Research Letters, 2019, 46, 179-188.	4.0	24
94	Compressional behavior of natural eclogitic zoisite by synchrotron X-ray single-crystal diffraction to 34 GPa. Physics and Chemistry of Minerals, 2019, 46, 333-341.	0.8	3
95	Fast identification of mineral inclusions in diamondÂat GSECARS using synchrotron X-ray microtomography, radiography and diffraction. Journal of Synchrotron Radiation, 2019, 26, 1763-1768.	2.4	9
96	lce-VII inclusions in diamonds: Evidence for aqueous fluid in Earth's deep mantle. Science, 2018, 359, 1136-1139.	12.6	166
97	Pressure-induced photoluminescence of MgO. Journal of Physics Condensed Matter, 2018, 30, 194002.	1.8	5
98	Phase Transitions in Orthoenstatite and Subduction Zone Dynamics: Effects of Water and Transition Metal Ions. Journal of Geophysical Research: Solid Earth, 2018, 123, 2723-2737.	3.4	20
99	Highâ€Pressure Geophysical Properties of <i>Fcc</i> Phase FeH _X . Geochemistry, Geophysics, Geosystems, 2018, 19, 305-314.	2.5	37
100	High-Capacity Sodium Peroxide Based Na–O ₂ Batteries with Low Charge Overpotential via a Nanostructured Catalytic Cathode. ACS Energy Letters, 2018, 3, 276-277.	17.4	15
101	Valence and spin states of iron are invisible in Earth's lower mantle. Nature Communications, 2018, 9, 1284.	12.8	35
102	Suppression of the magnetic order in CeFeAsO: Nonequivalence of hydrostatic and in-plane chemical pressure. Physical Review B, 2018, 98, .	3.2	4
103	Equations of State and Anisotropy of Feâ€Niâ€Si Alloys. Journal of Geophysical Research: Solid Earth, 2018, 123, 4647-4675.	3.4	21
104	Correlation between Structural Changes and Electrical Transport Properties of Spinel ZnFe ₂ O ₄ Nanoparticles under High Pressure. ACS Applied Materials & Interfaces, 2018, 10, 42856-42864.	8.0	16
105	The high-pressure anisotropic thermoelastic properties of a potential inner core carbon-bearing phase, Fe7C3, by single-crystal X-ray diffraction. American Mineralogist, 2018, 103, 1568-1574.	1.9	14
106	Metalâ€ŧoâ€5emiconductor Transition and Electronic Dimensionality Reduction of Ca ₂ N Electride under Pressure. Advanced Science, 2018, 5, 1800666.	11.2	36
107	Red-emitting salicylaldehyde Schiff base with AIE behaviour and large Stokes shift. Chinese Chemical Letters, 2018, 29, 1493-1496.	9.0	35
108	Universal link of magnetic exchange and structural behavior under pressure in chromium spinels. Physical Review B, 2018, 97, .	3.2	24

#	Article	IF	CITATIONS
109	Pressure Impact on the Crystal Structure, Optical, and Transport Properties in Layered Oxychalcogenides BiCu <i>Ch</i> O (<i>Ch</i> = S, Se). Journal of Physical Chemistry C, 2018, 122, 15929-15936.	3.1	15
110	Superconducting and magnetic phase diagram of <mml:math xmlns:mml="http://www.w3.org/1998/Math/MathML"> <mml:mrow> <mml:msub> <mml:mi>RbEuFe</mml:mi> <m and <mml:math xmlns:mml="http://www.w3.org/1998/Math/MathML"> <mml:mrow> <mml:msub> <mml:mi>CsEuFe</mml:mi> <m at high pressure. Physical Review B, 2018, 98, .</m </mml:msub></mml:mrow></mml:math </m </mml:msub></mml:mrow></mml:math 	3.2	31
111	Irreversible phase transformation in a CoCrFeMnNi high entropy alloy under hydrostatic compression. Materials Today Communications, 2018, 14, 10-14.	1.9	37
112	Dehydrogenation of goethite in Earth's deep lower mantle. Proceedings of the National Academy of Sciences of the United States of America, 2017, 114, 1498-1501.	7.1	83
113	Sound velocity and density of magnesiowüstites: Implications for ultralowâ€velocity zone topography. Geophysical Research Letters, 2017, 44, 2148-2158.	4.0	48
114	Effects of water on P-V-T equation of state of pyrope. Physics of the Earth and Planetary Interiors, 2017, 267, 9-18.	1.9	9
115	Pressureâ€Induced Bandgap Optimization in Leadâ€Based Perovskites with Prolonged Carrier Lifetime and Ambient Retainability. Advanced Functional Materials, 2017, 27, 1604208.	14.9	167
116	Sodium Peroxide Dihydrate or Sodium Superoxide: The Importance of the Cell Configuration for Sodium–Oxygen Batteries. Small Methods, 2017, 1, 1700102.	8.6	34
117	Making a fine-scale ruler for oxide inclusions. American Mineralogist, 2017, 102, 1969-1970.	1.9	0
118	High Pressure Single Crystal Diffraction at PX^2. Journal of Visualized Experiments, 2017, , .	0.3	35
119	Single-crystal equations of state of magnesiowüstite at high pressures. American Mineralogist, 2017, 102, 1709-1717.	1.9	9
120	Highâ€Pressure <i>γ</i> â€CaMgSi ₂ O ₆ : Does Pentaâ€Coordinated Silicon Exist in the Earth's Mantle?. Geophysical Research Letters, 2017, 44, 11,340.	4.0	18
121	Thermal Equation of State of Natural Tiâ€Bearing Clinohumite. Journal of Geophysical Research: Solid Earth, 2017, 122, 8943-8951.	3.4	12
122	Comparing the Pressure-Induced Structural Behavior of CuCr ₂ O ₄ and CuCr ₂ Se ₄ Spinels. Journal of Physical Chemistry C, 2017, 121, 16513-16520.	3.1	10
123	Experimental evidence for the survival of augite to transition zone depths, and implications for subduction zone dynamics. American Mineralogist, 2017, 102, 1516-1524.	1.9	11
124	Isosymmetric pressureâ€induced bonding increase changes compression behavior of clinopyroxenes across jadeiteâ€aegirine solid solution in subduction zones. Journal of Geophysical Research: Solid Earth, 2017, 122, 142-157.	3.4	11
125	Thermoelastic properties of grossular–andradite solid solution at high pressures and temperatures. Physics and Chemistry of Minerals, 2017, 44, 137-147.	0.8	8
126	High-pressure compressibility and vibrational properties of (Ca,Mn)CO ₃ . American Mineralogist, 2016, 101, 2723-2730.	1.9	29

#	Article	IF	CITATIONS
127	Compressional behavior of omphacite to 47ÂGPa. Physics and Chemistry of Minerals, 2016, 43, 707-715.	0.8	9
128	High-pressure behavior of natural single-crystal epidote and clinozoisite up to 40 GPa. Physics and Chemistry of Minerals, 2016, 43, 649-659.	0.8	16
129	Simultaneous band-gap narrowing and carrier-lifetime prolongation of organic–inorganic trihalide perovskites. Proceedings of the National Academy of Sciences of the United States of America, 2016, 113, 8910-8915.	7.1	269
130	Temperature of Earth's core constrained from melting of Fe and Fe0.9Ni0.1 at high pressures. Earth and Planetary Science Letters, 2016, 447, 72-83.	4.4	55
131	Thermal equation of state of natural tourmaline at high pressure and temperature. Physics and Chemistry of Minerals, 2016, 43, 315-326.	0.8	18
132	Fault‣lip Distribution of the 1999MwÂ7.1 Hector Mine Earthquake, California, Estimated from Postearthquake Airborne LiDAR Data. Bulletin of the Seismological Society of America, 2015, 105, 776-790.	2.3	19
133	Fast temperature spectrometer for samples under extreme conditions. Review of Scientific Instruments, 2015, 86, 013105.	1.3	12
134	P-V-T equation of state of Ca3Cr2Si3O12 uvarovite garnet by using a diamond-anvil cell and in-situ synchrotron X-ray diffraction. American Mineralogist, 2015, 100, 588-597.	1.9	10
135	Compressibility and equation of state of beryl (Be3Al2Si6O18) by using a diamond anvil cell and in situ synchrotron X-ray diffraction. Physics and Chemistry of Minerals, 2015, 42, 529-539.	0.8	18
136	P–V–T equation of state of spessartine–almandine solid solution measured using a diamond anvil cell and in situ synchrotron X-ray diffraction. Physics and Chemistry of Minerals, 2015, 42, 63-72.	0.8	9
137	Hidden carbon in Earth's inner core revealed by shear softening in dense Fe ₇ C ₃ . Proceedings of the National Academy of Sciences of the United States of America, 2014, 111, 17755-17758.	7.1	96
138	Silylation of mechanically ground kaolinite. Clay Minerals, 2014, 49, 559-568.	0.6	14
139	Elasticity and lattice dynamics of enstatite at high pressure. Journal of Geophysical Research: Solid Earth, 2013, 118, 4071-4082.	3.4	29
140	High Pressure Elastic Behavior of Synthetic Mg ₃ Y ₂ (SiO ₄) ₃ Garnet up to 9 GPa. Advances in Materials Science and Engineering, 2013, 2013, 1-6.	1.8	8
141	Compressibility of mimetite and pyromorphite at high pressure. High Pressure Research, 2013, 33, 27-34.	1.2	5
142	Spin crossover equation of state and sound velocities of (Mg _{0.65} Fe _{0.35})O ferropericlase to 140 GPa. Journal of Geophysical Research, 2012, 117, .	3.3	32
143	Local structure variations observed in orthoenstatite at high pressures. American Mineralogist, 2011, 96, 1585-1592.	1.9	14
144	Patterning Mammalian Cells for Modeling Three Types of Naturally Occurring Cell–Cell Interactions. Angewandte Chemie - International Edition, 2009, 48, 8303-8305.	13.8	90

#	Article	IF	CITATIONS
145	Control of the morphology of micro/nanostructures of polycarbonate via electrospinning. Science Bulletin, 2009, 54, 2911-2917.	1.7	20
146	Thermal equation of state of natural chromium spinel up to 26.8 GPa and 628 K. Journal of Materials Science, 2008, 43, 5546-5550.	3.7	16
147	Stability and Thermoelasticity of Diaspore by Synchrotron X-ray Diffraction and Raman Spectroscopy. Frontiers in Earth Science, 0, 9, .	1.8	1